# Rheology and spatially resolved structure of cetyltrimethylammonium bromide wormlike micelles through the shear banding transition

Matthew E. Helgeson, Paula A. Vasquez,
Eric W. Kaler, and Norman J. Wagner[a)]

*Center for Neutron Science, Department of Chemical Engineering, University of Delaware, Newark, Delaware 19716*

(Received 27 September 2008; final revision received 11 December 2008)

**Synopsis**

We present the first combined study of spatially resolved structure and shear rheology for a model shear banding fluid comprised of cetyltrimethylammonium bromide wormlike micelles. Combining conventional rheometry, velocimetry, flow birefringence, and flow-small angle neutron scattering (flow-SANS) in the 1–2 (flow-gradient) plane of shear completely characterizes shear banding in the system and enables comparison of local flow kinematics to local segmental orientation and alignment within the bands. The Giesekus constitutive equation with stress diffusion is shown to successfully model the viscoelasticity, steady shear viscosity, and shear banding kinematics. Flow-SANS measurements in the 1–2 plane exhibit a critical alignment and orientation required for shear banding, followed by a first order orientational transition to a paranematic state in the high-shear band. Master curves of the segmental orientation and alignment are constructed by comparing the local structural features to the locally observed shear rate. The Giesekus-diffusion model successfully predicts the measured segmental orientation and alignment, connecting the microstructure to the macroscopic rheology and shear banding kinematics. In doing so, a stress-SANS rule is developed, analogous to the stress-optic rule, that relates micellar flow alignment to the shear and normal stresses. The results confirm that shear banding is driven by a nonequilibrium shear-induced isotropic-nematic transition and suggest that the underlying phase behavior of the material is important in determining fluid microstructure and rheology during banding. © *2009 The Society of Rheology.* [DOI: 10.1122/1.3089579]

25 October 2023 01:47:23

## I. INTRODUCTION

Shear banding has been observed in a variety of systems, including entangled polymer solutions [Boukany *et al.* (2008); Hu *et al.* (2007)], colloidal suspensions [Vermant and Solomon (2005)], and most prominently, wormlike micelles (WLMs) [Berret *et al.* (1994); Decruppe *et al.* (1995); Hu and Lips (2005); Rehage and Hoffmann (1991)]. In the latter, shear banding was proposed to explain the birefringent bands observed in Couette flow for concentrated micellar solutions [Decruppe *et al.* (1995)], concomitant with stress plateaus in steady shear rheology [Rehage and Hoffmann (1991)]. These birefringence bands have been shown by experiment [Fischer and Callaghan (2000); Hu and Lips (2005)] to arise from segregation of the flow into two fluid layers, one at a high

[a)]Author to whom correspondence should be addressed: electronic mail: wagnernj@udel.edu

© 2009 by The Society of Rheology, Inc.

shear rate and one at a low shear rate, that span the flow geometry. This shear banding phenomenon has been associated with a variety of nonlinear rheological phenomena, including wall slip in polymer solutions [Boukany *et al.* (2008)], yielding in colloidal suspensions [Holmes *et al.* (2004)], and strong shear thinning as well as shear-induced phase separation in a variety of micellar systems [Hu *et al.* (2008); Liberatore *et al.* (2008)].

Shear banding in complex fluids has attracted both significant theoretical and experimental interests as some aspects of its associated behavior can be captured, at least qualitatively, by nonmonotonic rheological constitutive equations. Recent reviews by Olmsted (2008) and Dhont and Briels (2008) describe the mathematical framework underlying some current approaches to describe shear banding. However, these models are phenomenological and are not derived from microscopic considerations. As a result, there is a broad array of proposed physical mechanisms by which shear banding occurs in specific experimental systems. For example, shear banding of wormlike micelles is often attributed to some combination of effects, including a nonmonotonic constitutive relation, shear-induced breakage of individual micelles, and shear-induced phase transitions (both first and second order). In fact, recent experimental evidence [Liberatore *et al.* (2006)] suggests the microstructural mechanisms leading to banding depend largely on the particular system studied. Nevertheless, various phenomenological models for shear banding have been proposed to describe shear banding [Fielding and Olmsted (2003); Rehage and Hoffmann (1991); Spenley *et al.* (1993); Vasquez *et al.* (2007); Zhou *et al.* (2008)], which typically capture a nonmonotonic constitutive relation and stress plateau selection by coupling of the rheological constitutive equation to mass balances [Azzouzi *et al.* (2005)], population balances [Vasquez *et al.* (2007); Zhou *et al.* (2008)], or nonequilibrium free energy expressions [Fielding and Olmsted (2003)]. Although recent experimental evidence has confirmed the underlying nonmonotonic stress-rate curve for many banding fluids [Hu *et al.* (2007); Yesilata *et al.* (2006)], rigorous validation of the proposed microstructural mechanisms and their resulting constitutive models remain elusive. This is primarily due to an inability to directly measure the fluid's microstructure and rheology in the individual shear bands during shear banding.

Recently, we have developed the ability to measure spatially resolved structural information under shear using a short gap Couette cell for small angle neutron scattering (SANS) measurements in the 1–2 (flow-gradient) plane of shear [Liberatore *et al.* (2006)]. These 1–2 plane flow-SANS measurements provide several capabilities lacking in other techniques to measure structure under shear [Douglass *et al.* (2008); Ganapathy and Sood (2008); Manneville *et al.* (2007)]: (1) the size ranges accessible by SANS cover the relevant microstructural scales of wormlike micellar networks (e.g., micelle radius, persistence length, mesh size, etc.); (2) measurements in the 1–2 plane yield both the net segmental orientation and degree of alignment, whereas more common measurements in the 1–3 plane only measure a projection of the degree of alignment [Cappelaere *et al.* (1997)]; (3) the ability to collimate the neutron beam into a very thin slit provides gap-resolved measurements of the structure, which allows determination of the microstructure under flow in both the high-shear and low-shear bands during banding. Previous studies using this technique have elucidated the mechanism of shear banding for two different surfactant systems: aqueous solutions of erucyl bis-hydroxyethylmethylammonium chloride (EHAC) with sodium salicylate (NaSal) [Liberatore *et al.* (2006)] and cetylpyridinium chloride (CPyCl) with NaSal and NaCl [Wagner *et al.* (2005)]. These studies determined the mechanism of banding to depend on equilibrium phase behavior of the surfactant solution. For example, shear banding in EHAC-NaSal mixtures is associated with shear-induced phase separation [Liberatore *et al.* (2006); Schubert *et*

25 October 2023 01:47:23

*al.* (2004)], where the high shear band is comprised of a phase separated mixture of a brinelike phase and a dense network phase and has poorer shear-alignment than a non-banding composition of equivalent viscosity [Liberatore *et al.* (2008)]. On the other hand, shear banding in CPyCl-NaSal-NaCl is attributed to formation of a highly aligned state in the high-shear band which shows considerable spatial density fluctuations. These results suggest that shear banding is intimately linked to the underlying phase behavior of the fluid.

A limitation of the previous work is that both the EHAC and CPyCl systems shear banded over a range of shear rates such that experimental limitations prevented full exploration of the microstructure in the high-shear band. This work focuses on a third wormlike micellar system, aqueous cetyltrimethylammonium bromide (CTAB), near the isotropic-nematic (I-N) phase boundary [Cappelaere *et al.* (1995); Cappelaere *et al.* (1997); Hertel and Hoffmann (1988)]. Early measurements using flow birefringence [Cappelaere *et al.* (1995); Cappelaere and Cressely (1997); Decruppe *et al.* (1995)] suggested that CTAB compositions near the equilibrium I-N transition exhibit shear banding, which was later confirmed using velocimetry measurements [Becu *et al.* (2004); Fischer and Callaghan (2000; 2001)]. This has led to the hypothesis that shear banding in this system is due to a shear-induced I-N transition. However, the only evidence for such a transition is based solely on comparison of flow alignment in the 1–3 (flow-vorticity) plane that is convoluted across the structures formed in both bands [Cappelaere *et al.* (1997)]. In this work, we choose to study a specific composition near the equilibrium I-N phase boundary using a combination of 1–2 plane flow-SANS with conventional rheometry, particle imaging velocimetry (PIV), and flow-birefringence and dichroism. This allows for the first spatially resolved study of shear banding WLMs, including separate measurements of the high-shear and low-shear bands through the shear banding transition as well as characterization of the microstructure at shear rates beyond shear banding. Connecting these measurements through the use of a microstructurally based constitutive model allows for a quantitative link between fluid rheology and microstructure that can be used to evaluate the mechanism of shear banding.

25 October 2023 01:47:23

## II. RHEOLOGY OF SHEAR BANDING WORMLIKE MICELLES

### A. The Giesekus-diffusion model

The rheology in both simple shear and uniaxial extension of WLM solutions has been previously established [Yesilata *et al.* (2006)] to be well described by the Giesekus constitutive equation [Giesekus (1982)]. Although the original Giesekus model can predict a nonmonotonic stress-rate relation, it cannot predict the stress at which shear banding occurs without the addition of a forcing term. Augmenting the constitutive model with an empirical gradient diffusion term [Bhave *et al.* (1991)] enables selection of the stress condition for banding and the associated critical shear rates defining the banding regime. Recent work has discussed the implications of gradient diffusion in either the stress or deformation rate, which give rise to different predictions for the selected stress in the shear banded state [Olmsted (2008); Rossi *et al.* (2006)]. Here, we consider stress diffusion, where the total stress is given by

$$\boldsymbol{\tau} = \boldsymbol{\tau}_p + \eta_\infty \dot{\boldsymbol{\gamma}}, \tag{1}$$

with

$$\boldsymbol{\tau}_p^{(1)} + \left(\mathbf{I} + \frac{\alpha}{G_0}\boldsymbol{\tau}_p\right) \cdot \boldsymbol{\tau}_p - 2G_0\lambda\,\dot{\gamma} - \lambda D_\tau \nabla^2 \boldsymbol{\tau}_p = 0, \tag{2}$$

where $\boldsymbol{\tau}_p$ is the polymeric contribution to the total stress, $\eta_\infty$ is the limit of the viscosity at high shear rate, $\alpha$ is the drag-anisotropy coupling parameter, $G_0$ is the plateau modulus, $\lambda$ is the characteristic relaxation time, $\dot{\gamma} = \nabla\mathbf{v} + (\nabla\mathbf{v})^{\mathbf{T}}$ is the shear rate, and $D_\tau$ is the stress diffusivity. The superscript (1) represents the upper convected derivative of the polymeric stress. Here, stress diffusion is defined by the Laplacian term in Eq. (2). Under simple shear flow, the Giesekus-diffusion (G-D) model reduces to the following set of differential equations:

$$\lambda\frac{\partial \tau_{p11}}{\partial t} + \tau_{p11} + \frac{\alpha}{G_0}(\tau_{p11}^2 + \tau_{p12}^2) - \lambda D_\tau\left(\frac{\partial^2 \tau_{p11}}{\partial r_1^2} + \frac{\partial^2 \tau_{p11}}{\partial r_2^2}\right) = 0, \tag{3}$$

$$\lambda\frac{\partial \tau_{p22}}{\partial t} + \tau_{p22} - 2\lambda\,\dot{\gamma}\tau_{p12} + \frac{\alpha}{G_0}(\tau_{p22}^2 + \tau_{p12}^2) - \lambda D_\tau\left(\frac{\partial^2 \tau_{p22}}{\partial r_1^2} + \frac{\partial^2 \tau_{p22}}{\partial r_2^2}\right) = 0, \tag{4}$$

$$\lambda\frac{\partial \tau_{p12}}{\partial t} + \tau_{p12} - \lambda\,\tau_{p11}\dot{\gamma} + \frac{\alpha}{G_0}(\tau_{p11} + \tau_{p22})\tau_{p12} - \lambda D_\tau\left(\frac{\partial^2 \tau_{p12}}{\partial r_1^2} + \frac{\partial^2 \tau_{p12}}{\partial r_2^2}\right) - G_0\lambda\,\dot{\gamma} = 0, \tag{5}$$

where $r_1$ and $r_2$ represent the primary directions 1 and 2, respectively. For steady state viscometric flow, Eqs. (3)–(5) yield a constitutive shear stress-shear rate curve for the fluid; this will henceforth be referred to as "viscometric" model prediction. Viscometric predictions in the absence of stress diffusion predict a monotonically increasing stress for $0 < \alpha < 0.5$ and a nonmonotonic stress for $0.5 < \alpha < 1$. In the latter case, the addition of stress diffusion results in the recovery of monotonic behavior with a small, positive slope over the region in which shear banding occurs.

In the small-strain limit, the linear viscoelasticity predicted by the G-D model is that of a single-element Maxwell fluid with an additional viscous term representing the high shear viscosity

$$G'(\omega) = \frac{G_0(\lambda\omega)^2}{1 + (\lambda\omega)^2} \quad \text{and} \quad G''(\omega) = \frac{G_0(\lambda\omega)}{1 + (\lambda\omega)} + \eta_\infty\omega, \tag{6}$$

where $\omega$ is the applied frequency and the term $\eta_\infty\omega$ arises from the high-shear viscosity.

The Giesekus model is derived from a preaveraged description of the flow of bead-spring chains with anisotropic bead friction [Wiest and Bird (1986)]. It uses a Kramers expression for the microstructural contribution to the stress, described by the end-to-end vector $\mathbf{Q}$, through the ensemble-averaged second order conformation tensor

$$\langle\mathbf{QQ}\rangle = \mathbf{I} + \frac{\boldsymbol{\tau}_p}{G_0}. \tag{7}$$

In turn, the order tensor $\mathbf{S}$ describing the deviation of the normalized orientational conformation of the chains relative to the quiescent state is given by [Giesekus (1982)]

$$\mathbf{S} = \frac{\langle\mathbf{QQ}\rangle}{\mathrm{tr}\langle\mathbf{QQ}\rangle} - \frac{1}{3}\mathbf{I}. \tag{8}$$

Note that $\mathbf{S}$ is traceless as defined for incompressible flow. Because $\boldsymbol{\tau}_p$ and thus $\langle\mathbf{QQ}\rangle$ and $\mathbf{S}$ are symmetric, the order tensor can be decomposed into a unique set of orthonormal

25 October 2023 01:47:23

eigenvectors, **u**, and associated eigenvalues, $m$ (satisfying $\mathbf{S}=m\mathbf{Iu}$), that can be represented geometrically as an oriented ellipsoid. The average segmental orientation is the principal eigenvector of **S**, whose projection in the 1–2 plane of shear gives the average orientation angle, $\phi_0$, given by [Larson (1999)]

$$\cot 2\phi_0 = 2\left(\frac{S_{22}-S_{11}}{S_{12}}\right) = 2\left(\frac{\tau_{22}-\tau_{11}}{\tau_{12}}\right). \tag{9}$$

Here, $\phi_0=45°$ represents a system with orientation along the extension axis of the shear field, whereas $\phi_0=0°$ represents a system oriented along the shear direction. Similarly, one can express the degree of alignment along the principal direction by the eigenvalues of **S**, which are

$$m_1 = \frac{S_{11}+S_{22}+\sqrt{(S_{11}-S_{22})^2+4S_{12}^2}}{2}, \tag{10}$$

$$m_2 = \frac{S_{11}+S_{22}-\sqrt{(S_{11}-S_{22})^2+4S_{12}^2}}{2}, \tag{11}$$

$$m_3 = S_{33}, \tag{12}$$

where the eigenvalues are presented here in order of decreasing magnitude. Note that, as **S** is traceless, the sum of the eigenvectors must also identically be zero.

In principle, these eigenvalues allow for unique determination of a scalar order parameter, $S$, that reflects the degree of orientational order within the fluid with respect to the principal axis. However, the literature show disagreement in a standard definition for $S$ depending on the type of system studied. For example, in numerical simulations of rodlike liquids [Eppenga and Frenkel (1984); Vasanthi *et al.* (2001)], $S$ is defined such that $S=3/2|m_1|$. In contrast, in describing the rheology of polymeric fluids, $S=|m_1-m_2|=3/2(\mathbf{S}:\mathbf{S})^{1/2}$ is typically used [Joo *et al.* (2002); Larson, 1999]. Here, we propose a new parameterization of the orientational order to compare directly to the quantity measured by scattering measurements in the 1–2 plane, i.e., the distribution of segmental orientations. We define a scalar alignment factor $A_f$ (so as to avoid confusion with the order parameter $S$) as the sum of the eigenvalues of **S** in the 1–2 plane, such that

$$A_f = 3|m_1+m_2| = 3|S_{11}+S_{22}| = \frac{\tau_{11}+\tau_{22}}{3G_0+\tau_{11}+\tau_{22}}. \tag{13}$$

Here, $A_f$ is normalized such that $A_f=0$ corresponds to an isotropic fluid and $A_f=1$ corresponds to a perfectly aligned fluid. Thus, the alignment factor represents the degree of anisotropy of the fluid relative to the quiescent fluid.

### B. Flow kinematics in Taylor–Couette flow

The steady state velocity profiles for the G-D fluid can be calculated by solving Eqs. (3)–(5) simultaneously with the equations of motion, which for simple shear in cylindrical coordinates become

$$\left(\frac{1}{r}\frac{\partial(r\tau_{rr})}{\partial r}-\frac{\tau_{\theta\theta}}{r}\right)+\frac{\partial P}{\partial r}=0, \tag{14}$$

25 October 2023 01:47:23

$$\frac{1}{r^2}\frac{\partial(r^2\tau_{r\theta})}{\partial r} = 0, \tag{15}$$

where we have assumed negligible inertial contributions to the momentum. For an incompressible fluid, conservation of mass yields the continuity equation

$$\nabla \cdot \mathbf{v} = 0. \tag{16}$$

The equations of motion and continuity can be solved for the relevant velocity profile, $v_\theta(r)$, where $\theta$ and $r$ are substituted for the principal directions 1 and 2, respectively, in Eqs. (3)–(5), given appropriate boundary conditions. For Taylor–Couette flow, we assume no-slip boundary conditions between two concentric cylinders with inner and outer radii of $R_1$ and $R_2$, respectively,

$$v_\theta(R_1) = \frac{(R_2 - R_1)}{R_2/R_1}\dot{\gamma}_0, \tag{17}$$

$$v_\theta(R_2) = 0, \tag{18}$$

where $\dot{\gamma}_0$ is the nominal apparent shear rate.

Gradient stress diffusion in the constitutive equation requires boundary conditions for the stress. The type of stress boundary conditions chosen has been shown to influence the selection of the stress condition for shear banded flow, as well as give rise to "slippage" of the stress selection between various stable branches of the steady state stress [Rossi *et al.* (2006)]. Here, we choose Neumann boundary conditions for the stress, such that

$$\left.\frac{\partial(\boldsymbol{\tau})}{\partial r}\right|_{r=R_1} = \left.\frac{\partial(\boldsymbol{\tau})}{\partial r}\right|_{r=R_2} = 0. \tag{19}$$

The full set of differential equations for the G-D model defined by Eqs. (1), (3)–(5), and (14)–(16) using the boundary conditions (17)–(19) are solved using the Crank–Nicolson scheme described elsewhere [Zhou *et al.* (2008)] to obtain predictions for the various components of the stress as well as the resulting velocity profiles for inhomogeneous Taylor–Couette flow. Predictions obtained using this method will henceforth be referred to as "inhomogeneous" model predictions (in contrast to the viscometric predictions described previously for a fixed value of shear rate).

## III. MATERIALS AND METHODS

### A. Materials

The micellar solution studied in this work is a 16.7 wt % (490 mM) solution of CTAB (Acros Organics) in deuterium oxide ($D_2O$, 99.9%, Cambridge Isotope Laboratories) at 32 °C. Note that this composition is different from those used for previous studies [Becu *et al.* (2004); Cappelaere *et al.* (1997); Fischer and Callaghan (2000; 2001)] and was chosen due to the absence of significant fluctuations in steady state rheology. A solution of 21.3 wt % (570 mM) CTAB in $D_2O$, which is a nematic phase below 33 °C [Cappelaere *et al.* (1997)], was used to compare to SANS measurements to the shear banding sample. To prepare the solutions, dry CTAB powder was added to $D_2O$ in the appropriate amounts to a glass bottle. The bottle was agitated to disperse the powder and then placed in a temperature controlled water bath held at 32 °C. All experiments carried out on the sample were also performed at 32 °C. At this concentration, CTAB exhibits a Krafft temperature of approximately 27 °C [Hertel and Hoffmann (1988)], as well as an I-N phase boundary near the experimental conditions [Cappelaere *et al.* (1997)]. Care was

25 October 2023 01:47:23

taken in order to ensure the sample experienced no large excursions from 32 °C in order to prevent phase separation or recrystallization of the material. For PIV measurements, the solution was seeded with 100 ppm neutrally buoyant hollow spherical silica particles ($D=10$ $\mu$m, TSI Inc.). At these concentrations, the measured rheology is not significantly affected by the presence of the imaging particles.

### B. Rheometry

Rheological characterization of the CTAB solution was performed on two different rheometers. The first was a TA Instruments AR-G2 stress controlled rheometer using a Couette geometry with a moving inner cylinder of $R_1=15.5$ mm and a stationary outer cylinder of $R_2=16.0$ mm used for similarity to the flow geometries used in PIV, flow birefringence and dichroism, and flow-SANS measurements. Temperature was maintained with a Peltier-controlled outer cylinder held at 32 °C and a solvent trap wetted with $D_2O$ prevented solvent evaporation during measurement. A Rheometrics ARES strain controlled rheometer was also used with an upper 50 mm 0.04 rad cone and lower Peltier plate geometry in order to obtain reliable normal stress data. The results presented here for the steady shear rheology are not significantly influenced by the choice of rheometer or flow geometry.

The linear viscoelastic (LVE) and the steady state shear rheologies of the CTAB solution were measured on the AR-G2 rheometer using the following protocol. The sample was first given a preshear of 10 $s^{-1}$ for 60 s then allowed to rest for 100 s to ensure proper loading. LVE behavior was then measured by performing a frequency sweep at 5% strain from 200 to 1 rad/s and then another from 1 to 200 rad/s to check for hysteresis. Subsequently, the steady shear rheology was measured using a steady state rate sweep from 1 to 2500 $s^{-1}$, followed by another rate sweep from 2500 to 1 $s^{-1}$. Steady state stress sweeps were then performed from 40 to 100 Pa and from 100 to 40 Pa to compare the applied rate behavior to applied stress behavior.

### C. Particle imaging velocimetry

Flow-kinematic measurements using PIV were carried out using a device described previously [Hu and Lips (2005)]. The flow geometry consists of a Couette cell with an anodized aluminum inner cylinder with $R_1=17.0$ mm and an outer quartz cup with $R_2=17.5$ mm. The sample containing the imaging particles is loaded and given preshear similar to that used in the steady state rheology measurements. PIV measurements are performed by imaging the particles using a sheet laser incident on the quartz outer cylinder, which is reflected by the imaging particles and collected using a charge coupled device (CCD) camera. A measurement is performed by stepping the applied shear rate of the rheometer from rest to the desired rate. Subsequently, the shear stress is measured over time by the rheometer and the CCD camera takes consecutive image pairs once every second. Each image pair is then analyzed using a standard particle tracking algorithm [Azzouzi *et al.* (2005)] to yield the fluid velocity $v_\theta(r)$ as a function of the gap coordinate $r$. Data were taken for 60 s at each shear rate and steady state velocity profiles were obtained by averaging the PIV data over ten different image pairs recorded after the shear stress had achieved steady state (typically after approximately 20 s).

### D. Flow birefringence

Flow birefringence and dichroism were acquired with the optical analyzer module on a Rheometrics ARES rheometer using a Couette cell with $R_1=15$ mm, $R_2=17$ mm, and a total path length through the sample of 20 mm. The temperature of the Couette cell was

25 October 2023 01:47:23

held constant at 32 °C using a heating coil comprised of copper tubing with an inner diameter of 50 mm and a height of 60 mm placed concentrically around the Couette cup. Rheo-optical properties were measured for the CTAB solution under stepped flow conditions using the following procedure. The first interval was performed under no applied shear for 60 s followed by a second interval of stepped flow to the desired shear rate in the clockwise direction for 120 s. Cessation of shear for a third interval of 60 s was followed by a fourth interval of stepped flow at the previous shear rate in the counterclockwise direction for 120 s to ensure no bias toward the direction of flow. Finally, the shearing was stopped and optical measurements were made at rest for a final 60 s. Optical measurements at a given shear rate were averaged over the entire shear interval and over both directions of shear, resulting in average optical properties for the desired applied shear rate.

### E. Flow-SANS in the 1–2 plane of shear

Flow-SANS experiments in the 1–2 plane of shear were conducted at the NIST Center for Neutron Research on the NG-3 30 m SANS instrument. Scattering experiments were performed with neutrons with a wavelength of 6 Å (11% full width at half maximum, FWHM) at a sample to detector distance of 2.5 m. Measurements were made using an aluminum short gap Couette flow cell described previously [Liberatore *et al.* (2006)]. The shear cell consists of an inner rotating cylinder with $R_1 = 25.11$ mm and an outer stationary cup with $R_2 = 26.46$ mm. The cell temperature is controlled using a flow-through port within the cell that is connected to a controlled ethylene glycol bath. Two beam slits are placed prior to the front wall of the shear cell. The first, oriented horizontally with respect to the primary beam, is a 0.5 mm slit which constrains the scattering volume to the region of flow in the vertical direction. The second beam slit, oriented vertically with respect to the primary beam, is a 0.1 mm slit, which is mounted on a stepper motor allowing horizontal translation, yielding spatial resolution of the scattering volume at various positions across the Couette gap. The motor position is calibrated by measuring the total transmitted neutron counts over the range of motor positions while the cell is empty. Due to the large decrease in neutron transmittance between aluminum and fluid, the boundaries of the Couette gap are easily identified [Liberatore *et al.* (2006)].

After loading the CTAB solution and performing the same preshear protocol described previously, steady shear flow-SANS experiments were performed at several shear rates ranging from 0 to 2350 $s^{-1}$, which span the shear banding transition. SANS spectra were recorded for 15 min each at seven evenly spaced gap positions ranging from $r/H = 0.1$ to $r/H = 0.9$ for each applied shear rate. Transmission measurements were also performed at several shear rates (including 0 $s^{-1}$) at the positions closest to the inner and outer walls of the Couette gap for normalization of the scattering data. All experiments were performed such that the exterior cell temperature was 32 °C. In order to ensure that the sample scattering was not significantly influenced by the shear cell geometry, SANS spectra were also taken at rest for the CTAB sample in a standard titanium scattering cell with a 2 mm path length, placed in the 10CB sample environment for temperature control at 32 °C.

For comparison, flow-SANS measurements were also taken on a solution of 570 mM CTAB at 29 °C, which is in the nematic phase, using the following procedure. After loading into the shear cell, the sample scattering was measured at rest at three different gap positions. The sample was then sheared at 10 $s^{-1}$ for 5 min to uniformly orient the nematic phase, after which scattering was again measured at rest at the previous three gap

25 October 2023 01:47:23

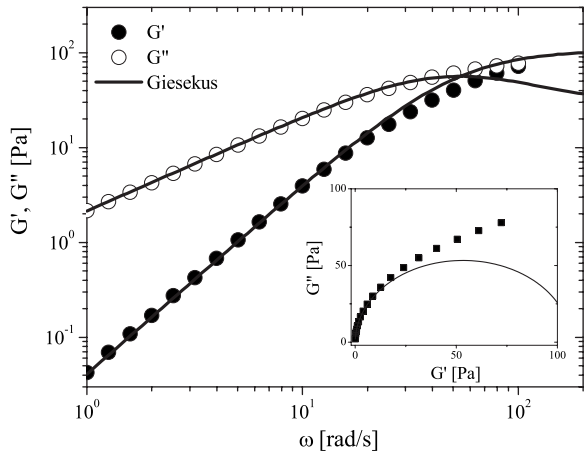


**FIG. 1.** Linear viscoelastic moduli for 16.7 wt % CTAB in $D_2O$ at 32 °C. Lines give fits to Eq. (6). Inset shows Cole–Cole representation of the data and fit.

positions. The resulting SANS data were reduced and normalized using standard methods [Glinka *et al.* (1998)] in order to produce absolute scattering intensity data in order to obtain quantitative information.

## IV. RESULTS

### A. Rheology and flow-kinematics

#### *1. Shear rheology*

The linear viscoelasticity of the 16.7 wt % CTAB solution at 32 °C is shown in Fig. 1. The behavior of $G'$ and $G''$ is indicative of an entangled wormlike micellar solution [Cates and Candau (1990)]. A Cole–Cole representation of the data clearly shows the CTAB sample to have non-Maxwellian behavior, as has been previously established for compositions near the I-N transition [Cappelaere *et al.* (1997)]. The steady state shear viscosity and shear stress are presented in Fig. 2 as a function of the nominal applied shear rate, $\dot{\gamma}_0$. Data obtained using the AR-G2 rheometer in both stress-controlled and strain-controlled modes are shown, and quantitative agreement is obtained between the two. The shear stress data obtained in strain-controlled mode show three characteristic regions: (i) linear growth of the stress in the zero-shear plateau, (ii) a region of almost zero slope where $\eta \sim \dot{\gamma}^{0.038}$ over a considerable range in shear rate henceforth referred to as the stress plateau, followed by (iii) an upturn in the shear stress as it approaches the limiting high-shear viscosity. This behavior is consistent with what has been previously observed in CTAB solutions of similar concentration [Cappelaere *et al.* (1997); Fischer and Callaghan (2001)] as well as in other micellar [Liberatore *et al.* (2006)] and polymer [Hu *et al.* (2007)] solutions, where the stress plateau is typically attributed to shear banding of the micellar solution. Finally, the steady state first normal stress difference, $N_1$, is shown in Fig. 3. At low shear rates, $N_1 \sim \dot{\gamma}_0^2$ as expected in the low-shear plateau [Gortemaker *et al.* (1976)], whereas it increases with a weaker dependence in the stress plateau.

The shear rheology of the CTAB solution is fit to the G-D model with $D_\tau = 0$ to yield the viscometric constitutive curve for the fluid as follows. The best fit values of $G_0 = 112 \pm 4$ Pa and $\lambda = 0.0185 \pm 0.0005$ s were determined from linear viscoelastic data for $G'$ and $G''$ (Fig. 1) using Eq. (6). The non-Maxwellian behavior is evident in deviations

25 October 2023 01:47:23

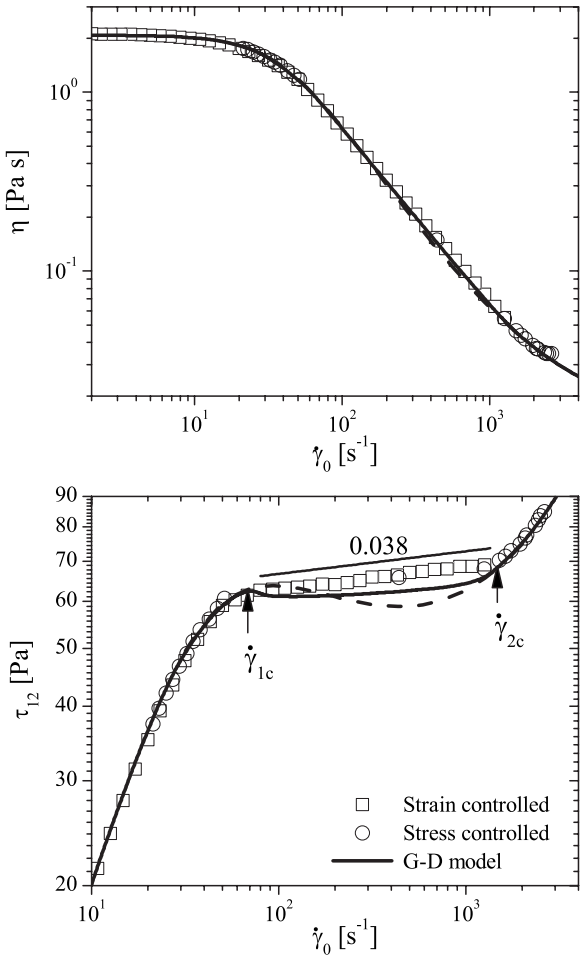


**FIG. 2.** Steady state shear viscosity (top) and stress (bottom) for 16.7 wt % CTAB in $D_2O$ at 32 °C. Both strain controlled (squares) and stress controlled (circles) measurements are shown. Lines give corresponding predictions from the G-D model under viscometric (dashed) and inhomogeneous (solid) flow.

from the model fit at high frequencies. Previous studies have extended the analysis to use multiple-mode Maxwell models in order to capture this high frequency behavior [Miller and Rothstein (2007)]. Here, the focus is on the nonlinear rheology and so, as will be shown, the single mode Giesekus model (with stress diffusion) is sufficient for this purpose.

The predicted value of the zero-shear rate viscosity $\eta_0 = G_0\lambda = 2.07 \pm 0.13$ Pa s is in good quantitative agreement with the measured value of 2.11 Pa s from steady shear rheology. Next, the parameters $\alpha$ and $\eta_\infty$ are fit to the steady state viscosity data holding all other parameters fixed at the previously stated values. The fit is performed on the stress-controlled data only, so as to not be influenced by the magnitude and slope of the stress plateau. This completes the fitting of model parameters for the Giesekus model without stress diffusion, and parameter values are summarized in Table I.

Viscometric predictions for $\tau_{r\theta}(\dot{\gamma}_0)$, $\eta(\dot{\gamma}_0)$, and $N_1(\dot{\gamma}_0)$ were computed by solving Eqs. (3)–(5) (with $D_\tau = 0$), and the results are given by the dotted lines in Figs. 2 and 3. The value of $\alpha = 0.895 \pm 0.005$ and resulting nonmonotonic behavior of the underlying visco-

25 October 2023 01:47:23

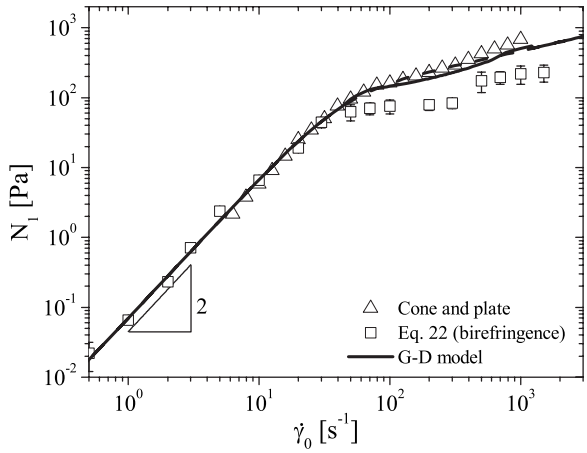


**FIG. 3.** First normal stress difference under steady shear for 16.7 wt % CTAB in $D_2O$ at 32 °C. Closed and open symbols represent measurements made on a cone and plate rheometer and predictions from birefringence using Eq. (22), respectively. Lines give corresponding predictions from the G-D model under viscometric (dashed) and inhomogeneous (solid) flow.

metric constitutive curve suggest that the CTAB solution is indeed shear banding at shear rates in the stress plateau. The nonmonotonic constitutive curve displays a stress maximum at $\lambda\dot{\gamma}_0 \sim 1.7$, which is significantly lower than that predicted by previous models of shear banding [Spenley *et al.* (1993)]. Independent validation of the model fits is made by comparing the viscometric predictions for $N_1$ to the experimentally measured values under steady shear obtained using a cone and plate geometry. Figure 3 shows excellent quantitative agreement between the model predictions and experiment up to shear rates in the stress plateau. The Giesekus model slightly underpredicts $N_1$ in the stress plateau, as has also been observed in other WLMs [Liberatore *et al.* (2008)].

### 2. Particle imaging velocimetry

PIV data were collected at several shear rates encompassing the stress plateau and the resulting average steady state velocity profiles are plotted in Fig. 4. The PIV measurements allow for clear definition of the flow-kinematic behavior in regions I, II, and III. In region I, the velocity profiles are nearly linear and thus, the shear rate is nearly homogeneous across the gap. After a lower critical shear rate, $\dot{\gamma}_{1c}$, the velocity profile is clearly nonhomogeneous at nominal shear rates ranging from 100 to 1500 $s^{-1}$, indicating shear

**TABLE I.** Giesekus fit parameters and predictions.

| Parameter | Symbol | Fit value |
|---|---|---|
| Zero-shear viscosity | $\eta_0$ | $2.07 \pm 0.13$ Pa s |
| Plateau modulus | $G_0$ | $112 \pm 4$ Pa |
| Relaxation time | $\lambda$ | $0.0185 \pm 0.005$ s |
| Anisotropy parameter | $\alpha$ | $0.895 \pm 0.004$ |
| High-shear viscosity | $\eta_\infty$ | $0.015 \pm 0.001$ Pa s |
| Stress diffusion coefficient | $D_\tau$ | $0.9 \pm 0.2 \times 10^{-8}$ $m^2/s$ |
| Lower critical shear rate | $\dot{\gamma}_{1c}$ | 65.0 $s^{-1}$ |
| Upper critical shear rate | $\dot{\gamma}_{2c}$ | 1480 $s^{-1}$ |

25 October 2023 01:47:23

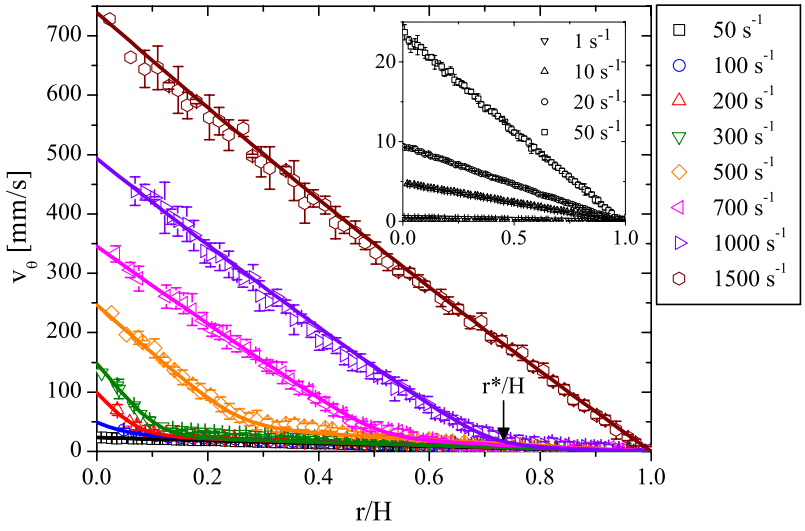


**FIG. 4.** Velocity profiles measured by PIV under steady shear for 16.7 wt % CTAB in $D_2O$ at 32 °C for the applied shear rates indicated between $\dot{\gamma}_{1c}$ and $\dot{\gamma}_{2c}$. Inset graph shows data for applied shear rates less than $\dot{\gamma}_{1c}$. Lines show predictions from G-D model for inhomogeneous flow, where $D_\tau$ was obtained by fitting to the profile at 100 $s^{-1}$.

banding. This observation is in agreement with previous velocimetry measurements using nuclear magnetic resonance (NMR) on solutions of different composition [Fischer and Callaghan (2001)]. Finally, after an upper critical shear rate, $\dot{\gamma}_{2c}$, a nearly linear velocity profile is again observed, marking the completion of shear banding. It should be noted that no fluctuations in the velocity profiles are observed beyond the measurement uncertainty. This is in contrast to previously reported data on a sample that is closer to the I-N transition [Becu *et al.* (2004)] which show considerable fluctuations as well as wall slip in measured velocity profiles in the shear banded state. This suggests that the magnitude of spatiotemporal fluctuations in CTAB depends strongly on the relative proximity of the fluid to the equilibrium I-N transition.

The location of the interface between the high-shear and low-shear bands, $r^*/H$ (where $H=R_2-R_1$) is mathematically defined by the location where the local shear rate, defined by $\dot{\gamma}(r)=r(d/dr)(v_\theta/r)$, exhibits a clear discontinuity. Figure 5 shows a plot of $r^*/H$ versus the nominal applied shear rate, which exhibits a linear increase from 0 to 1 over shear rates in the stress plateau. Also shown in Fig. 5 are the average local shear rates in the high shear band ($r<r^*$) and low shear band ($r>r^*$) calculated from the PIV data. These average shear rates increase mildly through the stress plateau at increasing applied shear rates, except very close to $\dot{\gamma}_{1c}$ and $\dot{\gamma}_{2c}$ where large variations are observed due to the small number of data points (and large associated uncertainty) in the high- and low-shear bands, respectively. Finally, in region III, a homogeneous velocity profile is observed. Here, the velocity profile exhibits a smoothly varying shear rate across the Couette gap, which has been shown to correspond to significant shear thinning of the fluid [Hu *et al.* (2008); Liberatore *et al.* (2008)].

To model the flow kinematics of the shear banding CTAB solution, the PIV data at a nominal shear rate of 100 $s^{-1}$ are fit to the inhomogeneous form of the G-D model. All model parameters are fixed at the values in Table I, with $D_\tau$ as the only adjustable parameter. This is illustrated in Fig. 6, where the dimensionless velocity $v_\theta(r)/v_\theta(R_1)$ is plotted versus $r/H$ for several values of the dimensionless stress diffusivity $\delta=\lambda D_\tau/H^2$.

25 October 2023 01:47:23

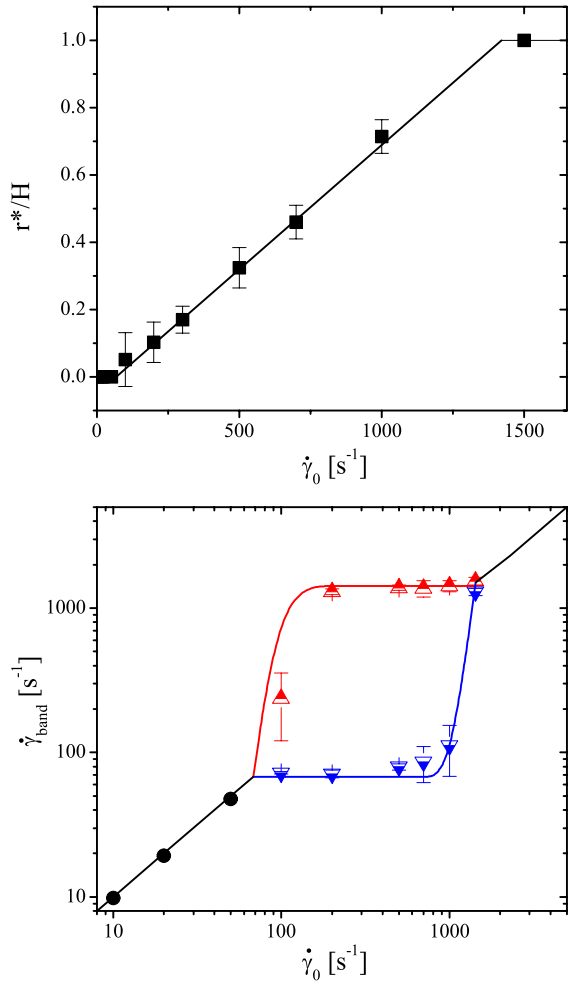


**FIG. 5.** (Top) Location of the shear band interface and (bottom) local shear rates in the high (>) and low (≅) shear bands versus applied shear rate determined from PIV measurements. Lines give predictions from the G-D model.

The standard error of the predicted velocity profile is minimized at a value of $\delta$=0.001, resulting in a fit value of $D_\tau = 0.9 \pm 0.2 \times 10^{-8}$ m$^2$/s. This value of $D_\tau$ is used along with the previously fit parameters in Table I to predict the remaining measured velocity profiles. The solid lines in Figs. 4–6 show that these results are in excellent quantitative agreement with the experimental data and demonstrate that no wall slip occurs in the shear banded state. Figure 5 shows that $r^*/H$, the location of the shear band interface, is accurately predicted by the G-D model, as well as the average shear rates in the high shear and low shear bands. This allows for quantitative definition of the upper and lower critical shear rates, $\dot{\gamma}_{1c}$ and $\dot{\gamma}_{2c}$, as the applied shear rate at which bifurcation in the predicted shear stress begins and ceases to occur, respectively [Rossi *et al.* (2006)]. For the 16.7 wt % CTAB solution at 32 °C, we obtain $\dot{\gamma}_{1c}$=65.0 s$^{-1}$ and $\dot{\gamma}_{2c}$=1480 s$^{-1}$.

Determination of the stress diffusion coefficient enables prediction of the stress that would be measured in the Couette cell experimentally in the shear banding regime. Specifically, the selected stress is determined by a combination of the form of the gradi-

25 October 2023 01:47:23

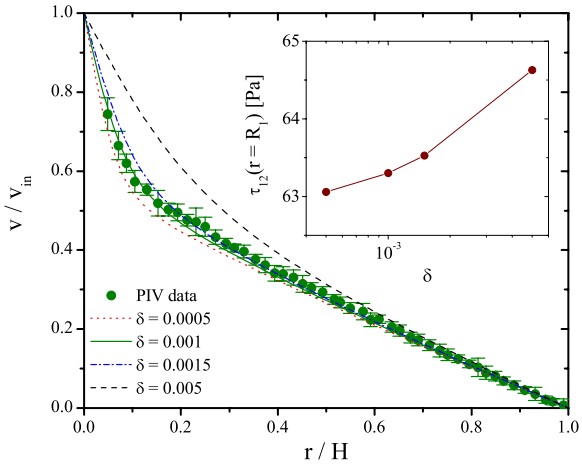


**FIG. 6.** Dependence of the velocity profile predicted by the G-D model on the stress diffusivity for a nominal applied shear rate of 100 $s^{-1}$. Points are experimental data from PIV, whereas lines are predictions of the model for various values of $\delta$. Inset graph shows the predicted wall shear stress.

ent term in Eq. (2), its coefficient $D_\tau$, the boundary conditions used on the stress gradients, and the geometrical parameters $R_1$ and $R_2$ [Rossi *et al.* (2006)]. The inset in Fig. 6 shows the wall shear stress predicted by the G-D model at $\dot{\gamma}_0 = 100\ s^{-1}$ for various values of $\delta$, where the selected stress increases with increasing stress diffusivity. The solid line in Fig. 2 shows the predictions for the wall shear stress, $\tau_{r\theta}|_{r=0}$, for the G-D model with the best-fit parameters in Table I. The model accurately predicts the selected stress at $\dot{\gamma}_{1c}$. At $\dot{\gamma}_0 \sim 100\ s^{-1}$, the inhomogeneous G-D model predicts a jump to lower shear stresses, which has been shown to result from the choice of boundary conditions in solving the inhomogeneous flow problem [Rossi *et al.* (2006)]. The G-D model predicts a power law exponent in the shear banding regime of 0.030, which is slightly smaller than that measured experimentally. This may be attributed to the choice of boundary conditions on the stress, an underprediction by the G-D model of the sensitivity of the selected stress to the chosen geometry, or a combination thereof.

## B. Structural measurements

### *1. Rheo-optics*

The average transmittance, $T$, and dichroism, $\Delta n''$, birefringence magnitude, $\Delta n'$, and extinction angle, $\chi$, of the shear banding CTAB sample were measured for applied shear rates spanning the shear banding transition. As the incident laser spot size is nearly the size of the Couette cell gap, these quantities are averaged over the varying flow kinematics in the gap. Thus, during banding, the rheo-optical measurements represent an average of both the low-shear and high-shear bands. Figure 7 shows the steady state rheo-optical properties for a wide range of applied shear rates. The CTAB sample exhibits no significant decrease in transmission over the entire range of shear rates, in contrast to other shear banding fluids that exhibit significant turbidity during shear banding [Schubert *et al.* (2004)]. At shear rates below $\dot{\gamma}_{1c}$, the sample also exhibits no significant dichroism. However, the dichroism increases significantly after $\dot{\gamma}_{1c}$, suggesting flow-induced anisotropic fluctuations large enough to scatter light are generated in the material in the shear banding regime.

25 October 2023 01:47:23

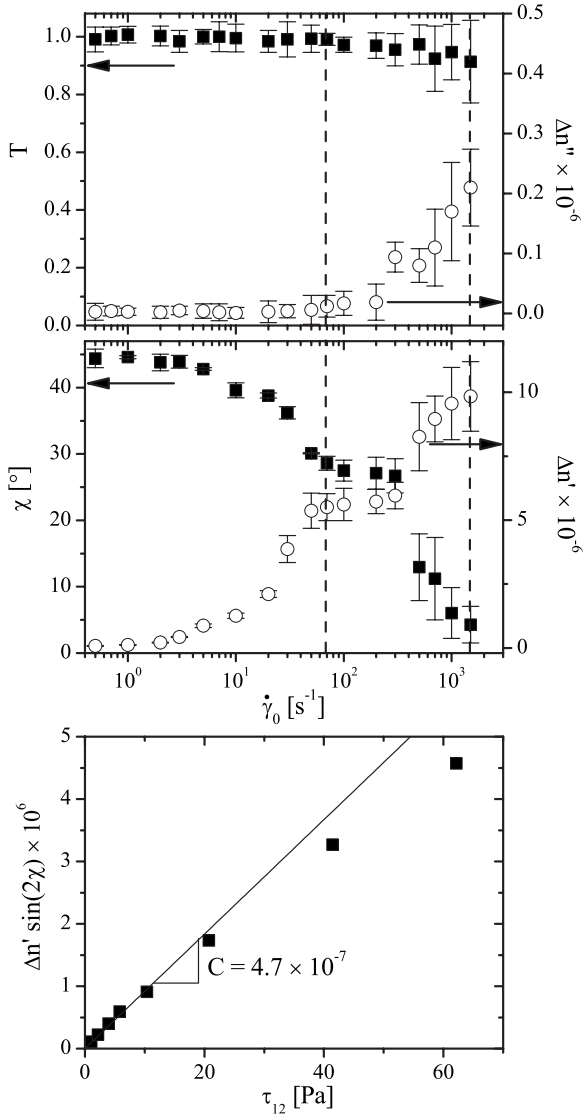


**FIG. 7.** (Top) Total transmittance (closed symbols) and dichroism (open symbols), as well as (middle) extinction angle (open symbols) and birefringence (closed symbols) of 16.7 wt % CTAB in $D_2O$ at 32 °C versus nominal applied shear rate. Dotted lines mark the lower and upper critical shear rates for shear banding. (Bottom) Determination of the stress-optic coefficient at low shear rates.

At low shear rates, the extinction angle approaches 45°, as expected for an isotropic, randomly oriented fluid. For shear rates below $\dot{\gamma}_{1c}$, $\chi$ decreases and $\Delta n'$ increases monotonically, indicating alignment and stretching of micellar chains due to shear. For applied shear rates near and above $\dot{\gamma}_{1c}$, the extinction angle and birefringence continue to decrease and increase, respectively, but with a much smaller slope, similar to what was observed by Cappelaere *et al.* (1997). However, as the applied shear rate is increased further toward $\dot{\gamma}_{2c}$, an apparent discontinuity in $\chi$ and $\Delta n'$ is observed, upon which the extinction angle decreases significantly and the birefringence increases significantly with increasing applied shear rate. This apparent discontinuity can be attributed to the aver-

25 October 2023 01:47:23

**TABLE II.** Structural parameters for 490 mM CTAB in $D_2O$.

| Parameter | Symbol | Method | Value |
|---|---|---|---|
| Volume fraction | $\phi$ | | 0.18 |
| Surfactant density (solid) | $\rho$ | | 1.064 g/cm$^3$ |
| Neutron contrast | $\Delta\rho_s$ | | $5.8\times10^{-6}$ Å$^{-1}$ |
| Micellar radius | $r_{cs}$ | SANS | $2.03\pm0.05$ nm |
| Radius polydispersity (FWHM) | $\Delta r/r$ | SANS | $0.176\pm0.03$ |
| Persistence length | $l_p$ | Birefringence | $40.3\pm1.8$ nm |
| Mesh size | $\xi_m$ | Rheology | $33.5\pm1.2$ nm |
| Contour length | $L_c$ | Rheology | $223\pm18$ nm |
| Lower critical orientation | $\phi_{1c}$ | flow-SANS | 22.8° |
| Upper critical orientation | $\phi_{1c}$ | flow-SANS | 4.6° |
| Lower critical alignment | $A_{1c}$ | flow-SANS | 0.09 |
| Upper critical alignment | $A_{2c}$ | flow-SANS | 0.52 |

aging of the rheo-optic data over a substantial part of the gap, such that the beam switches between probing primarily the low shear band to primarily the high shear band as it grows to fill the gap with increasing shear rate. Approaching $\dot{\gamma}_{2c}$, the extinction angle approaches 0° and the birefringence is significant, showing that the fluid structure above $\dot{\gamma}_{2c}$ is flow aligned. At sufficiently low shear rates, the stress-optic rule is expected to hold, where the shear and normal stresses are expected to follow

$$\tau_{12} = \frac{1}{2C}\Delta n' \sin(2\chi), \tag{20}$$

$$N_1 = \frac{1}{C}\Delta n' \cos(2\chi), \tag{21}$$

where $C$ is the stress-optic coefficient, which must be empirically fit to the data. Figure 7 shows a plot of Eq. (20), whose slope yields $C=4.6\times10^{-7}$ Pa$^{-1}$. Predictions of $N_1$ from Eq. (21) are compared to the rheological measurements in Fig. 3. The data show that for sufficiently low shear rates the rheo-optical data satisfy both Laun's rule [Gortemaker *et al.* (1976)], where $N_1\sim\dot{\gamma}_0^2$, as well as the stress-optic rule. The stress-optic rule fails at an applied shear rate approximately equal to $\dot{\gamma}_{1c}$, where similar deviations are also observed in the shear stress (Fig. 7).

The stress-optic coefficient can be used [Schubert *et al.* (2003)] to estimate the persistence length, $l_p=40.3\pm1.8$ nm, of the CTAB micelles using previously reported values for the optical properties of CTAB in water [Shikata *et al.* (1994)]. Determination of the persistence length allows for estimation of other structural properties of entangled WLMs, such as the mesh size, $\xi_m$, and the contour length, $L_c$, of the micelles given values of $G_0$ and the local minimum in $G''$ at high frequencies [Cates and Candau (1990)]. Using the fit value of $G_0$ and the local minimum in $G''$ predicted by Eq. (6), this yields values of $\xi_m=33.5\pm1.2$ nm and $L_c=223\pm18$ nm. This value of the mesh size merely represents an upper bound for the micellar solution, as it is estimated assuming Maxwellian behavior of the fluid. Thus, the CTAB micelles are found to be short and fairly rigid compared to other WLMs of interest [Liberatore *et al.* (2008); Schubert *et al.* (2003)] and highly entangled. These results are summarized in Table II, which lists the relevant length scales measured for the CTAB sample.

25 October 2023 01:47:23

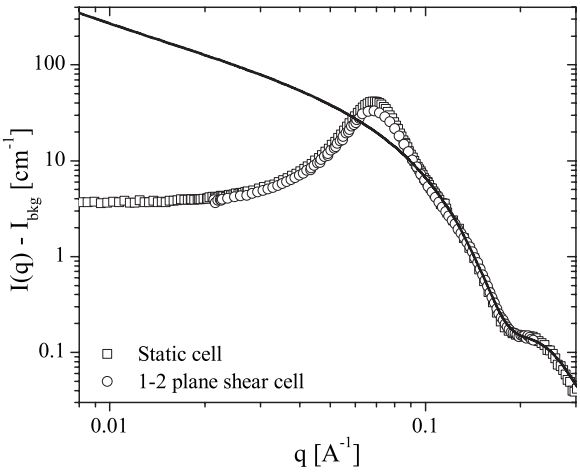


**FIG. 8.** Absolute scattered intensity versus scattering vector $q$ for 16.7 wt % CTAB at 32 °C at rest obtained in the 1–2 plane shear cell (circles) as compared to a standard titanium scattering cell (squares). Line gives prediction using a model for flexible cylinders using the parameters shown in Table II.

### *2. Flow-SANS in the 1–2 plane*

Figure 8 shows the circularly averaged absolute scattered intensity (with incoherent background subtracted), $I(q)$-$I_{\text{bkg}}$, from the 16.7 wt % CTAB sample at rest at 32 °C in both the standard titanium scattering cell and the 1–2 plane shear cell. Overall, good quantitative agreement is observed between two different scattering environments. The scattering displays a correlation peak at $q_{\max}=0.069$ Å$^{-1}$ due to the strong unscreened segment-level electrostatic interactions between micelles leading to liquidlike order [Cannavacciuolo *et al.* (2002)]. This makes fitting of the data to obtain structural parameters difficult. The scattering model proposed by Cannavacciuolo *et al.* (2002) can be used to model such interactions, but failure of the model at high volume fractions prevents description of the SANS data for the current system. With this in mind, a simpler model for noninteracting flexible cylinders with polydisperse cylindrical cross section [Pedersen and Schurtenberger (1996)] was used to fit the SANS data at $q>0.1$ Å$^{-1}$ to obtain the micellar radius, $r_{\text{cs}}$, and polydispersity, $\Delta r/r$. The contour length was fixed at $L_c=223$ nm and the Kuhn length at $b=2l_p=80.6$ nm. This results in fit values of $r_{\text{cs}}=2.03\pm0.05$ nm and $\Delta r/r=0.176\pm0.03$. These results are summarized in Table II, and the scattering fit is shown as the solid line in Fig. 8.

The fit micellar radius is slightly smaller than that measured in previous studies (~2.4 nm) for CTAB/NaSal wormlike micelles [Nettesheim *et al.* (2008); Shikata *et al.* (1994)], which is reasonable given the propensity of $\text{Sal}^-$ ions to associate with the hydrophilic shell of the micelles, thereby increasing the micellar radius [Imae (1990)]. The relatively short contour length compared to the Kuhn length ($L_c/b\sim3$) suggests that the micelles are relatively inflexible compared to systems with screened electrostatic interactions [Schubert *et al.* 2003]. The measured scattering shows significant deviations from the fit for $q<0.1$ Å$^{-1}$. The observed deviations are qualitatively consistent with Monte Carlo simulations of WLMs with strong electrostatic interactions in an unscreened environment [Cannavacciuolo *et al.* (2002)], similar to the situation of concentrated CTAB in the absence of electrolyte studied here.

Figure 9 shows the reduced two-dimensional scattered intensity contours for all gap positions at nominal shear rates spanning $\dot{\gamma}_{1c}$ and $\dot{\gamma}_{2c}$ for the CTAB solution. Since no

25 October 2023 01:47:23

**FIG. 9.** (Color) Two-dimensional 1–2 flow-SANS patterns at the applied shear rates (coordinate axis) and normalized gap positions (ordinate axis) indicated. Inset line shows the location of the shear band interface, $r^*/H$, measured by PIV. The flow direction is shown for reference.

25 October 2023 01:47:23

measurable fluctuations were observed in the velocity profiles, the data are assumed to represent the stable steady state structure of the fluid through the shear banding transition. The solid line in the figure corresponds to the measured location, $r^*/H$, of the interface between the high-shear and low-shear bands measured by PIV. For shear rates below $\dot{\gamma}_{1c}$, a nearly isotropic ring is observed in the scattering, corresponding to the correlation peak at $1/q_{\max}$ observed in the circularly averaged data. This correlation ring corresponds to distances on the order of the persistence length or less and thus anisotropy of this ring corresponds to segmental alignment of the WLMs. For positions in the high shear band, significant anisotropy is observed, which progressively aligns with the flow direction as the local shear rate increases (lower right corner).

Two measures of segmental alignment are calculated: the average orientation of the micelles relative to the flow direction ($\phi_0$) and the degree of alignment of the segments about the primary orientation ($A_f$). These are calculated by performing an annular average of the scattered intensity around the correlation peak, $I(q_{\max}, \phi)$, where $\phi$ is the azimuthal angle with respect to the flow direction. Thus, complete segmental alignment of the micelles along the flow direction would correspond to sharp peaks in $I(q_{\max}, \phi)$ at 90° and 270°. Figure 10 shows plots of $I(q_{\max}, \phi)$ at different values of $\dot{\gamma}_0$ at $r/H = 0.11$ (top) as well as different values of $r/H$ at $\dot{\gamma}_0 = 500\ \mathrm{s}^{-1}$ (bottom). At $r/H = 0.11$, the scattering anisotropy increases significantly with $\dot{\gamma}_0$ through the shear banding transition, while the intensity minima shift closer to 90° and 270° at shear rates near and above $\dot{\gamma}_{2c}$. Similar behavior is observed at different values of $r/H$ for $\dot{\gamma}_0 = 500\ \mathrm{s}^{-1}$, where the scattering anisotropy increases from the outer stationary wall to the inner rotating wall.

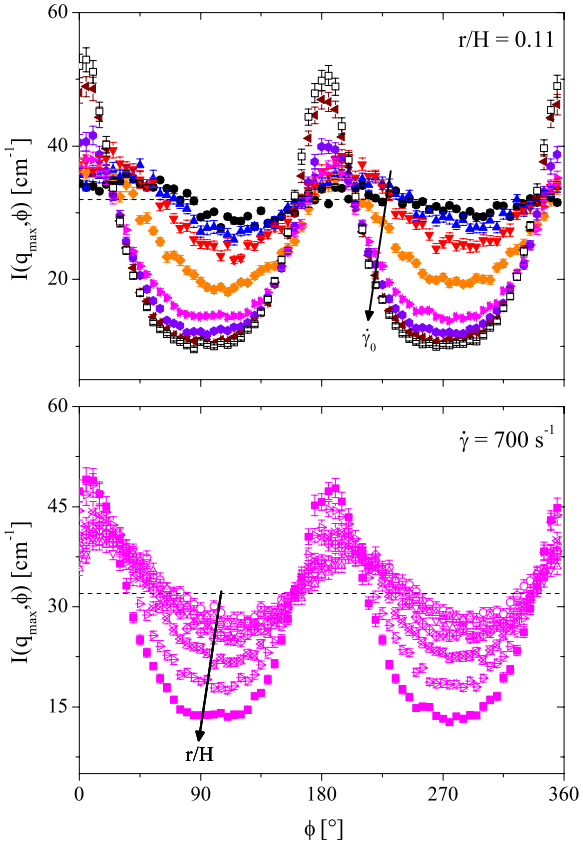


**FIG. 10.** Annular-averaged intensity at $q_{max}$ for (top) $r/H$=0.11 for the shear rates listed in Fig. 9 and (bottom) at $\dot{\gamma}_0$=700 s$^{-1}$ for the gap positions listed in Fig. 9. Dotted line corresponds to $I(q_{max})$ for $\dot{\gamma}_0$=0 s$^{-1}$.

Specifically, measurements in the low shear band show low alignment, whereas measurements in the high shear band show a greater degree of anisotropy, approaching complete flow alignment at the highest local shear rates.

The average segmental orientation, $\phi_0$, is given by the azimuthal angle corresponding to the minimum in the scattered intensity and is determined for each value of $\dot{\gamma}_0$ and $r/H$ by fitting the intensity curve using a method described previously [Liberatore *et al.* (2006)]. Figure 11 shows $\phi_0$ for positions across the Couette gap at shear rates spanning the entire shear banding transition. At low shear rates, the orientation is close to 45° and is relatively homogeneous across the gap, as expected for a WLM solution below $\dot{\gamma}_{1c}$ where the velocity field is nearly uniform and the shear rates relatively low in comparison to the fluid's longest relaxation time. However, in the shear banding transition between $\dot{\gamma}_{1c}$ and $\dot{\gamma}_{2c}$, the segmental orientation is nonhomogeneous in the high-shear band, with significantly higher flow alignment ($\phi_0 \rightarrow 0$) evident near the inner, rotating wall. The location at which this inhomogeneity begins coincides well with $r^*/H$ (shown as stars for each applied nominal shear rate). Furthermore, the value of the orientation angle at $r^*/H$ is relatively independent of shear rate, with an average value of $17 \pm 2°$. The orientation in the low-shear band is roughly independent of applied shear rate, whereas the orienta-

25 October 2023 01:47:23

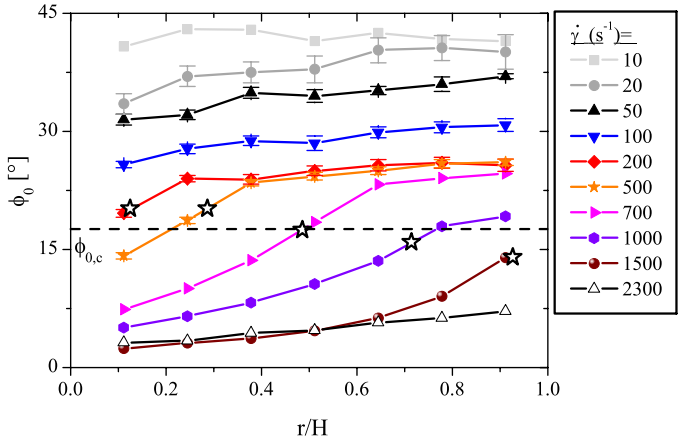


**FIG. 11.** Orientation angle versus normalized gap position measured using 1–2 plane flow-SANS for the applied shear rates indicated. Star symbols represent the location of $r^*/H$ at the corresponding applied shear rate. Dashed line indicates the average orientation at $r^*/H$.

tion of samples in the high-shear band tends toward flow alignment with increasing applied shear rate. At even higher shear rates ($\dot{\gamma}_0 > \dot{\gamma}_{2c}$), the orientation is nearly flow aligned everywhere in the Couette gap.

The degree of micellar alignment about the average orientation is determined by the alignment factor

$$A_f(q^*) = -\frac{\int_0^{2\pi} I(q^*,\phi)\cos(2(\phi-\phi_0))d\phi}{\int_0^{2\pi} I(q^*)d\phi}, \tag{22}$$

where $q^*$ is the $q$-value at which the integrals are calculated. The alignment factor is a two-dimensional analog to the order parameter for suspensions of rigid rods [Walker and

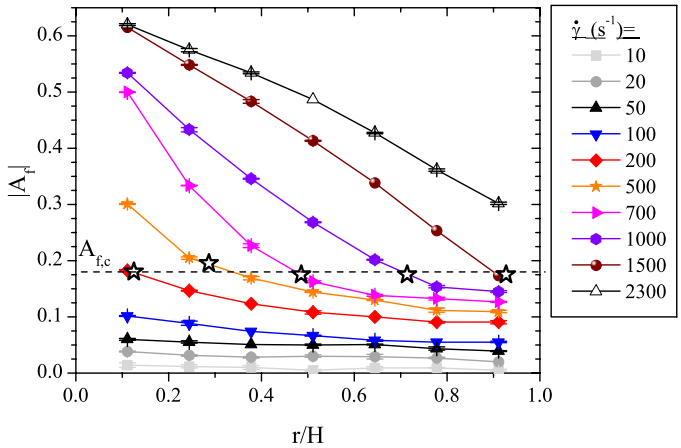


**FIG. 12.** Alignment factor versus normalized gap position measured using 1–2 plane flow-SANS for the applied shear rates indicated. Star symbols represent the location of $r^*/H$ at the corresponding applied shear rate. Dashed line indicates the average alignment at $r^*/H$.

25 October 2023 01:47:23

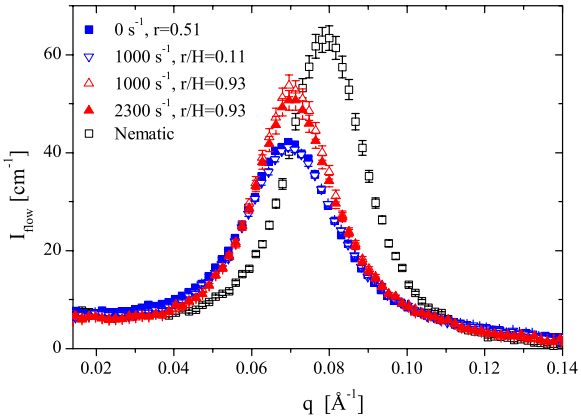


**FIG. 13.** Sector-averaged scattering in the flow direction for the applied shear rates and gap positions indicated. Open symbols show structure in the high-shear (8) and low-shear (c) bands (local shear rates are listed in the text). Also shown are data for a shear-aligned nematic phase at rest.

Wagner (1996)] and ranges between 0 (no alignment) and 1 (complete alignment) as defined. Figure 12 shows $A_f(q_{\max})$ corresponding to the data shown in Fig. 10. At shear rates below $\dot{\gamma}_{1c}$, the segmental alignment is nearly isotropic and uniform across the gap. For shear rates between $\dot{\gamma}_{1c}$ and $\dot{\gamma}_{2c}$, $A_f$ is inhomogeneous and increases sharply toward the inner rotating wall. Positions in the low shear band have similar alignment regardless of applied shear rate, and the point at which the sharp increase in $A_f$ begins coincides well with the value of $r^*/H$ measured using PIV (again marked with stars). As with the orientation angle, the value of $A_f$ at $r^*/H$ is roughly independent of applied shear rate, with an average value of $0.18 \pm 0.01$. For applied shear rates higher than $\dot{\gamma}_{2c}$, a smooth increase in $A_f$ from the outer to the inner wall is observed, similar to what is observed for materials that exhibit strong shear thinning but no shear banding [Liberatore *et al.* (2008)]. A maximum alignment near $A_f$=0.6 is achieved at shear rates near and above $\dot{\gamma}_{2c}$.

Beyond segmental orientation and alignment, SANS can also test for any underlying microstructural differences due to the applied flow. Sector averages of the scattered intensity were calculated over an azimuthal range of −45°–45° and are shown in Fig. 13. Representative results below $\dot{\gamma}_{1c}$ (at 0 s$^{-1}$), between $\dot{\gamma}_{1c}$ and $\dot{\gamma}_{2c}$ (at $\dot{\gamma}_0$=1000 s$^{-1}$), and above $\dot{\gamma}_{2c}$ (at 2300 s$^{-1}$) are plotted in Fig. 13. The data curves measured at $\dot{\gamma}_0$ =1000 s$^{-1}$ correspond to local shear rates for the high shear and low shear bands of 1430 and 74 s$^{-1}$, respectively. At 0 s$^{-1}$, the same correlation peak reported in Fig. 8 is seen, with an intensity maximum at $q_{\max}$=0.069 Å$^{-1}$. Contrastingly, at 2300 s$^{-1}$, the correlation peak of the flow-aligned material shows a significant increase in peak sharpness and intensity, suggesting a very high degree of order. For conditions in the shear banding regime, the scattering from positions in the low-shear band is quantitatively indistinguishable from the structure at rest, whereas the scattering from positions in the high-shear band is indistinguishable from the structure at shear rates above $\dot{\gamma}_{2c}$. This indicates that the microstructure in the low-shear band is similar to the fluid structure at rest, whereas the microstructure in the high-shear band resembles that of the material at shear rates beyond the shear banding transition. It should be noted that the features at $q$ values significantly lower and higher than the correlation peak remain unchanged regardless of applied shear rate or gap position, suggesting that (1) the cylindrical cross section of the micelles remains unchanged by the application of shear and (2) no large-scale structures

25 October 2023 01:47:23

(at least in the experimental window of SANS) are observed as a direct result of shear banding. This latter observation is in agreement with the maintenance of optical transmission throughout the shear banding transition and is in marked contrast to other shear banding micellar systems such as EHAC, which develop significant low-$q$ scattering and turbidity due to shear-induced phase separation that accompanies shear banding [Liberatore *et al.* (2006); Schubert *et al.* (2004)].

The flow-aligned microstructure exhibits scattering that is comparable to that of a nematic WLM fluid. For comparison, flow-SANS measurements were performed on a nematic sample of 21.3 wt % CTAB at 29 °C. The scattering from the nematic phase at rest after flow alignment yielded $\phi_0=0.7°$ and $A_f=0.58$, as noted by the solid lines in Figs. 11 and 12. These values are very similar to, and in some cases exceeded by, the values observed in the high-shear band and at shear rates above $\dot{\gamma}_{2c}$ in the shear banding 16.7 wt % CTAB sample. Similarly, the sector-averaged scattering of the nematic phase at rest (Fig. 13) shows a shift in $q_{\max}$ to higher $q$ as expected. Comparing to the shear banded sample suggests that the fluid microstructure in the high shear band, and at shear rates above $\dot{\gamma}_{2c}$, is consistent with a flow-aligned nematic, or "paranematic," phase as has been previously hypothesized [Cappelaere *et al.* (1997)].

## V. DISCUSSION

### A. Determination of shear banding and local rheological behavior

The velocimetry measurements for the 16.7 wt % CTAB sample at 32 °C confirm that the sample is indeed shear banding, in agreement with rheo-NMR measurement on a sample of similar, but not identical, composition [Fischer and Callaghan (2001)]. Except for applied shear rates very close to the two critical shear rates, the local shear rates observed within the shear bands are roughly constant and an apparent stress plateau is observed in the steady state rheology over this range in applied shear rate. This confirms that shear banding in the CTAB system can be thought of as the nonequilibrium rheological equivalent of thermodynamic phase separation [Dhont and Briels (2008)], where the fluid is unstable between $\dot{\gamma}_{1c}$ and $\dot{\gamma}_{2c}$ such that it segregates into two flow states, one at $\dot{\gamma}_{1c}$ (the low-shear band) and one at $\dot{\gamma}_{2c}$ (the high-shear band).

The relative amounts of these two states in a finite gap Couette flow are found to vary linearly with the applied shear rate, i.e., via a simple lever rule. This is in contrast to previous measurements by Cappelaere *et al.* (1997), where the amount of the gap occupied by the high-shear band was inferred to increase nonlinearly with increasing applied shear rate using flow-birefringence and 1–3 plane flow-SANS measurements. The former method assumes direct proportionality of the birefringence and local shear rate, which we have shown to be invalid by breakdown of the stress-optic law above $\dot{\gamma}_{1c}$. The latter method assumes that the convoluted scattering in the 1–3 plane is simply the spatial average of the gap-dependent structure, which has been shown to be invalid for other wormlike micellar systems [Liberatore *et al.* (2006)]. This discrepancy highlights both the importance of direct measurements of the flow kinematics, such as by PIV, as well as direct probing of the microstructure in the plane of flow (1–2) plane with spatial resolution so as to probe the microstructure in each band independently.

### B. Coupling of local rheology and orientational order

The structural profiles measured during shear banding in Figs. 11 and 12 show no discontinuity across the shear banding interface. Rather, positions in the low-shear band exhibit orientation and alignment that is roughly independent of applied shear rate, whereas the structure in the high-shear band evolves continuously toward a nematic-like

25 October 2023 01:47:23

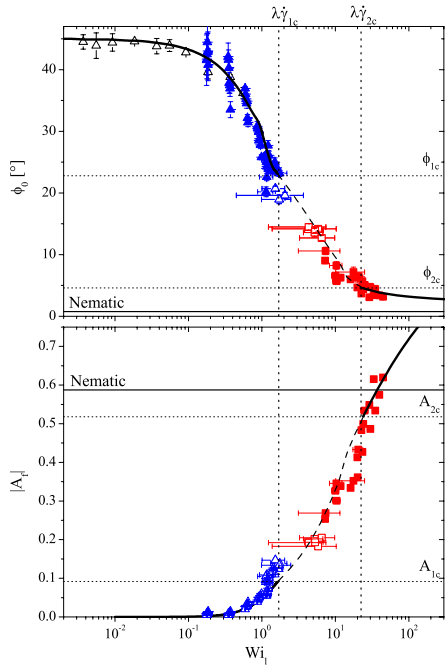


**FIG. 14.** Orientation angle (top) and alignment factor (bottom) versus local Weissenberg number. Triangles indicate positions in the low-shear band, whereas squares indicate positions in the high-shear band. Open symbols represent gap positions that contain $r^*/H$. The orientation angle is augmented at low shear rates using flow-birefringence data (open points). Curves give corresponding predictions from the G-D under inhomogeneous flow.

25 October 2023 01:47:23

state as the applied shear rate increases. This result seems to agree with previous measurements on the CPyCl-NaSal-NaCl system [López-González *et al.* (2006)], where the structure of micelles in the high-shear band was shown to vary continuously across the gradient direction.

This previous observation arises from examining the spatially dependent structure at a single applied shear rate. However, combining PIV measurements with spatially resolved flow-SANS measurements in the 1–2 plane allows for unique comparison of the *local* rheology and flow kinematics during shear banding to *local* fluid microstructure. To do so, we plot the measured structural parameters $\phi_0$ and $A_f$ obtained by gap-resolved flow-SANS measurements against the locally observed shear rate at the corresponding gap position measured by PIV in Fig. 14. To facilitate comparison to theories, the local shear rate is reduced to a local Weissenberg number, $Wi_l = \lambda \langle \dot{\gamma}(r) \rangle_{r+\Delta r}$, where $\langle \dot{\gamma}(r) \rangle_{r+\Delta r}$ is the average of the local shear rate over the experimental window defined by the slit width $\Delta r$ in the gap-resolved flow-SANS measurements. Half-filled points in Fig. 14 indicate where the shear band interface lies within the sample aperture for flow-SANS measurements, where the shape of the half-filled points represents the band in which the majority of the sample aperture lies. These points also have correspondingly large uncertainty in assigning the local shear rate. We also assign $\chi = \phi_0$, such that the orientation angle can be augmented by the flow-birefringence data at low shear rates, where lack of anisotropy in the SANS pattern precludes accurate determination of $\phi_0$. This results in unification of the SANS and rheo-optical data onto master curves of orientation and alignment.

Figure 14 shows that the orientation angle and alignment factor collapse onto single

master curves, demonstrating the utility in 1–2 plane flow-SANS measurements. In the low-shear branch (triangles), the orientation decreases and the alignment increases continuously until the onset of shear banding at $\dot{\gamma}_{1c}$, where a critical orientation of $\phi_{1c}$ and critical alignment of $A_{1c}$ are observed for points in the low-shear band. At this point (if one ignores points containing the shear band interface with large associated error), both the orientation and alignment undergo a discontinuous jump to a highly flow-aligned fluid in the high shear band (squares) with critical orientation of $\phi_{2c}$ and alignment of $A_{2c}$. These results show that the fluid undergoes a first order orientational transition to a paranematic state at critical values of the orientation angle and alignment factor, which segregate the structure observed in the high-shear and low-shear bands.

As discussed previously, the G-D model directly couples the orientational order of the fluid and the polymeric stress. As such, the orientation angle $\phi_0$ and alignment factor $A_f$ measured by flow-SANS are directly comparable to the quantities defined in Eqs. (9) and (13), respectively. With the model parameters in Table I, the G-D model predictions for $\phi_0$ and $A_f$ under inhomogeneous flow are given in Fig. 14 and are in excellent agreement with the experimentally obtained values measured using gap-resolved flow-SANS. Note that for $Wi_l$ corresponding to shear rates between $\dot{\gamma}_{1c}$ and $\dot{\gamma}_{2c}$, respectively, the shear stress and thus the structure are not unique due to stress bifurcation [Rossi *et al.* (2006)] and thus predictions in this range are indicated by a dotted line in Fig. 14 merely to guide the eyes.

Using the inhomogeneous form of the G-D model to calculate the orientation and alignment at $\dot{\gamma}_{1c}$ and $\dot{\gamma}_{2c}$, we find $\phi_{1c}=22.8°$, $\phi_{2c}=4.6°$, $A_{1c}=0.09$, and $A_{2c}=0.52$ (these values are listed in Table II). The numerical values of $\phi_{2c}$ and $A_{2c}$ are similar to those measured for the flow-aligned equilibrium nematic phase discussed previously. However, points in the high-shear band at local shear rates below $\dot{\gamma}_{2c}$ exhibit alignment that is far lower than that of the nematic phase, suggesting that the incipient flow-aligned structure in the high-shear band evolves continuously to a paranematic state as the local shear rate increases.

25 October 2023 01:47:23

### C. Microstructural mechanism for shear banding

The results of gap-resolved flow-SANS measurements, in combination with rheo-optical measurements, reveal that shear banding in the CTAB system results from a shear-induced isotropic-paranematic transition, as previously hypothesized by other investigators [Berret *et al.* (1994); Decruppe *et al.* (1995); Fischer and Callaghan (2001)]. Such a transition is akin to what is observed in suspensions of rigid rods, where coupling between hydrodynamics and rod orientation results in development of a paranematic state under shear [Dhont and Briels (2008)]. Indeed, given that the CTAB micelles explored here have contour lengths of only a few times the persistence length, one might expect such similarities to rodlike systems.

The proposed mechanism for shear banding in the CTAB system is as follows. Before the onset of shear banding, the fluid structure is nearly isotropic and homogeneous throughout the flow geometry. The onset of the shear banding occurs at $\dot{\gamma}_{1c}$, which corresponds to critical values of the orientational order of $\phi_{1c}$ and $A_{1c}$. At this point, the fluid undergoes a first order transition in orientation and alignment, resulting in the formation of a paranematic phase in the high-shear band at $\dot{\gamma}_{2c}$. For Couette flow, the high-shear band is located at the rotating inner cylinder where the shear stresses are higher. Here, the relevant condition for coexistence is $\tau_{12}(r^*/H^+)=\tau_{12}(r^*/H^-)$. Further increasing the applied shear rate above $\dot{\gamma}_{1c}$ results in the growth of the paranematic phase

at the expense of the isotropic phase according to the linear "mixing rule" observed in PIV measurements. Eventually, the entire gap is occupied by a paranematic phase with nematic-like order.

It should be noted that the stress condition for equilibrium does not necessitate a true plateau in the measured wall shear stress, as the curvature of the Couette geometry gives rise to a unique nonzero slope in the shear banded state [Olmsted (2008)]. This leads to the variations in both local shear rate and orientational order as observed in Fig. 11 and results in an incipient structure in the high shear band that is relatively unaligned compared to an equilibrium nematic phase. Note that the paranematic microstructure is very sensitive to small changes in the shear rate, as evinced by the steep slope in Fig. 14 around the banding transition. Combined results of gap-resolved flow-SANS and rheo-optics also suggest that both the high-shear and low-shear bands comprise two separate homogeneous phases as opposed to other systems exhibiting shear-induced phase separation where one of the shear bands is a two-phase mixture [Schubert *et al.* (2004); Liberatore *et al.* (2006)].

### D. An analogy to the stress-optic law for SANS

Given that $\phi_0$ and $A_f$ represent two independent scalar parameterizations of the order tensor **S**, it is reasonable to assume that the polymeric contributions to rheological material functions follow a "stress-SANS" rule similar to the stress-optic rule given by Eqs. (21) and (22). Here, we find

$$\tau_{12,p} = G_0(2.73A_f)^{1/2}\sin(2\phi_0), \tag{23}$$

$$N_{1,p} = G_0(2.73A_f)^{1/2}\cos(2\phi_0). \tag{24}$$

The leading coefficient of 2.73 on $A_f$ was determined by simultaneous comparison of the G-D model predictions of the right-hand sides of Eqs. (23) and (24) to the predicted values of the polymeric shear and normal stresses for $Wi \ll 1$. The power of 1/2 on the alignment factor is required to satisfy linear viscoelasticity and Laun's rule ($\tau_{12} \sim \dot{\gamma}$ and $N_1 \sim \dot{\gamma}^2$) in the low-shear limit. It should be noted that Eqs. (23) and (24) are only exact relationships in the limit of low shear rate and breakdown of the stress-SANS rule is expected for sufficiently nonlinear deformation, similar to the breakdown observed in the stress-optic rule. Figure 15 shows plots of the normalized shear stress and first normal stress difference predicted for viscometric flow using the G-D model along with the predictions from the stress optic rule [Eqs. (20) and (21)] and the stress-SANS rule [Eqs. (23) and (24)]. As with the stress-optic law, the stress-SANS predictions are accurate at shear rates below $\dot{\gamma}_{1c}$ and deviations from these relationships occur at shear rates above $\dot{\gamma}_{1c}$. Interestingly, the deviations of the stress-SANS and stress-optic rule at higher shear rates are qualitatively similar.

These results demonstrate verifiable structure-property relationships that directly couple the orientational order of the fluid measured by flow-SANS to the macroscopically observed material functions without the need to employ a constitutive model, similar to what has been long established for rheo-optical measurements of micellar and polymeric fluids [Lee *et al.* (2005); Shikata *et al.* (1994)]. Note that this approach does not require a proportionality constant that must be independently measured (i.e., the analogous stress-SANS coefficient is equal to unity), as flow-SANS is a direct measurement of the orientational order whereas flow birefringence is an indirect measurement via the dielectric properties of the fluid. Furthermore, the predictions of Eq. (22) allow direct observation of the nonmonotonic constitutive curve without presupposition of a particular

25 October 2023 01:47:23

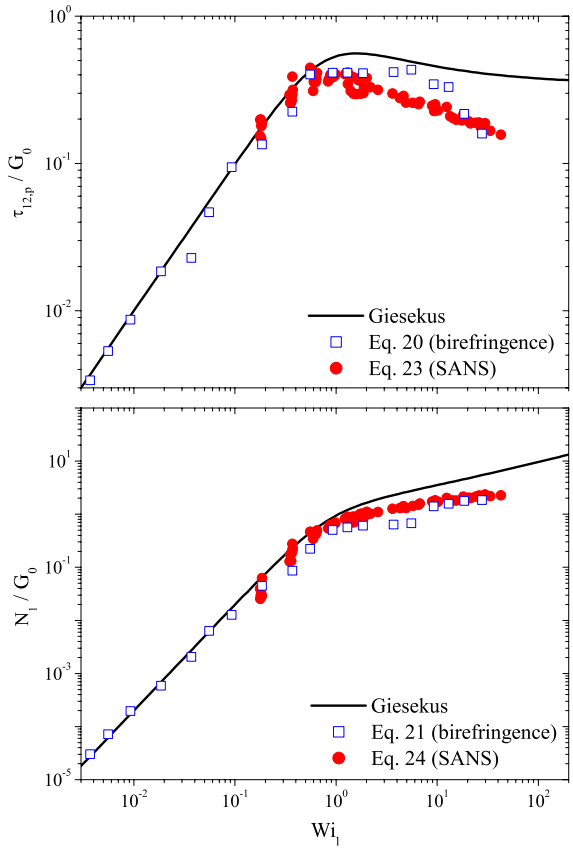


**FIG. 15.** Stress-SANS (circles) and stress-optic (squares) rule results for polymeric contributions to the steady state shear stress (top) and first normal stress difference (bottom). Solid lines represent viscometric predictions using the Giesekus model. Symbols represent predictions from flow-birefringence using Eqs. (20) and (21) and from 1–2 plane flow-SANS using Eqs. (23) and (24). (Note: birefringence data are plotted versus nominal applied Weissenberg number, $Wi = \lambda \dot{\gamma}_0$.)

constitutive model, which is required for other approaches [Boukany *et al.* (2008); Hu *et al.* (2007)]. This suggests that both flow-SANS and flow-birefringence measurements in the 1–2 plane allow for independent experimental verification of an underlying nonmonotonic constitutive relation, circumventing the problems associated with rheometry mentioned in the previously cited works [Hu *et al.* (2007); Olmsted (2008)].

### E. Constitutive modeling and the role of stress diffusion

Despite its simplicity relative to more recently proposed constitutive models [Vasquez *et al.* (2007); Zhou *et al.* (2008)], the Giesekus model with stress diffusion shows remarkable ability in describing the steady state rheology of the shear banding fluid and associated flow kinematics in Couette flow. Fitting the anisotropy parameter $\alpha$ to rheological data allows for direct determination of the underlying nonmonotonic constitutive curve. Note that the first normal stress difference is particularly sensitive to the value of $\alpha$ and provides an independent test of the fit. This suggests that fitting stress-controlled rheological data to the Giesekus model may be a simple yet sufficient approach for determining a given fluid to be shear banding or not in the absence of more complicated

25 October 2023 01:47:23

flow-kinematic measurements such as PIV (although the latter is admittedly the only way to truly discriminate shear banding and nonbanding fluids [Hu *et al.* (2008)]).

The incorporation of stress diffusion into the constitutive model allows for the determination of a unique stress plateau, an ability which is lacking in most simple models of shear banding [Dhont and Briels (2008); Spenley *et al.* (1993)], as well as accurate prediction of the flow kinematics through the shear banding transition. Furthermore, it allows for the prediction of a steep but continuous evolution of the local shear rate over the shear band interface, which is consistent with spatially resolved kinematic and structural measurements. However, the measured shear stresses and first normal stress differences during banding exhibit larger magnitude than those predicted by the model during shear banding, despite agreement in magnitude at the onset of banding. Future refinements of the model could include dependence of model parameters on thermodynamic variables, coupled with mass, population, or energy balance, as has already been performed for other models [Fielding and Olmsted (2003); Vasquez *et al.* (2007); Zhou *et al.* (2008)]. Additionally, the current work is limited in scope to steady state behavior of shear banding fluids. In order to more rigorously test model predictions, future efforts will seek to compare transient rheological and flow-kinematic measurements of the shear banding CTAB system to G-D model predictions for transient flows such as shear startup and large amplitude oscillatory shear and address the topic of fluctuations observed for samples closer to the equilibrium I-N transition [Becu *et al.* (2004)].

Although the incorporation of stress diffusion is mathematically practical in the constitutive modeling of shear banding fluids, convincing arguments as to the structural and physical origins of such gradient diffusion are lacking [Dhont and Briels (2008); Olmsted (2008)]. Bhave *et al.* (1991) originally proposed that stress diffusion arises from stress-induced gradients in the number density of chain segments, an approach which has recently been more explicitly considered to describe the reversible breakage of wormlike micelles [Vasquez *et al.* (2007)]. Here, the structural basis for stress diffusion is clearly evident, whereby spatial gradients in the polymeric stress arise from gradients in fluid microstructure between the high-shear and low-shear bands. Whether or not gradients in orientational order are further accompanied by gradients in the number density of micelles in solution remains unclear and will be the subject of future studies.

The results of this study also highlight the ability of the constitutive model to predict the experimentally observed orientational order of the fluid with excellent accuracy. To the authors' knowledge, this is the first attempt to quantitatively link measured fluid microstructure to rheology and flow kinematics of a shear banding fluid. The model provides a mathematical interpretation of the alignment factor measured by scattering measurements as the sum of the eigenvalues of the orientational order tensor in the 1–2 plane. Thus, this description of local fluid microstructure should be applicable for other polymeric fluids, such as highly entangled polymers [Hu *et al.* (2007)] and semiflexible chains [Boukany *et al.* (2008)], and other shear banding WLMs [Hu *et al.* (2008); Liberatore *et al.* (2006)].

## VI. CONCLUSIONS

Combination of rheological measurements with local flow-kinematic measurements (PIV) and local microstructural measurements using gap-resolved flow-SANS has identified the microstructural mechanism underlying shear banding in a model wormlike micellar fluid. For CTAB, shear banding results from a nonequilibrium first order shear-induced separation of the flow field into two distinct states of the material: a nearly isotropic micellar phase in the low-shear band and a flow-aligned paranematic state in the

25 October 2023 01:47:23

high-shear band, which becomes increasingly ordered with increasing local shear rate. The onset of banding occurs at critical values of the segmental orientation and alignment that are maintained at the shear banding interface. These results suggest that shear banding in micellar solutions is intimately connected to the underlying phase behavior of the material. Indeed, given similar results for other shear banding systems, one may hypothesize that shear banding in WLMs is a general consequence of nonequilibrium shear-induced phase transitions. With this in mind, further efforts to connect shear banding in the current system and other fluids of interest to the underlying equilibrium phase behavior of the material are under way.

The relatively simple Giesekus-diffusion model has been demonstrated to accurately describe not only the steady state rheology and flow kinematics during shear banding, but also the orientational order and alignment of the segments of the WLMs and their associated transitions during banding. The incorporation of gradient diffusion in the stress allows for unique selection of the stress plateau given an underlying nonmonotonic constitutive curve, as well as prediction of flow-kinematic profiles through the shear banding transition.

We also demonstrate a stress-SANS law from measurements in the 1–2 plane of shear to predict shear and normal stresses from direct SANS measurements of the microstructure under flow. These new structure property relationships allow for independent experimental verification of a nonmonotonic stress-rate constitutive curve and could potentially be applied similarly to investigate the underlying local microstructural constitutive behavior of a variety of polymeric and micellar fluids that exhibit shear banding.

25 October 2023 01:47:23

## ACKNOWLEDGMENTS

The authors thank D. Chandler, L. P. Cook, F. Nettesheim, and M. W. Liberatore for helpful discussions. We especially thank W. R. Burghardt for comments regarding model predictions of the structure. PIV measurements were performed with Y. T. Hu and assistance with flow-SANS experiments was provided by L. Porcar. The MATLAB code used for calculations using the G-D model was kindly provided by L. Zhou. This paper was prepared under Cooperative Agreement No. 70NANB7H6178 from the National Institute of Standards and Technology (NIST), U.S. Department of Commerce. The statements, findings, conclusions, and recommendations are those of the authors and do not necessarily reflect the views of NIST or the U.S. Department of Commerce. Financial support for this work was provided by Unilever, Inc. and the Delaware Center for Neutron Science. Some of the rheological measurements were performed on an instrument obtained under ARO Award No. W911NF-05-1-0234. Any opinions, findings, and conclusions or recommendations expressed in this material are those of the author(s) and do not necessarily reflect the views of the Army Research Office.

## References

Azzouzi, H., J. P. Decruppe, S. Lerouge, and O. Greffier, "Temporal oscillations of the shear stress and scattered light in a shear-banding-shear-thickening micellar solution," Eur. Phys. J. E **17**, 507–51C4 (2005).

Becu, L., S. Manneville, and A. Colin, "Spatiotemporal dynamics of wormlike micelles under shear," Phys. Rev. Lett. **93**, 018301 (2004).

Berret, J. F., D. C. Roux, and G. Porte, "Isotropic-to-nematic transition in wormlike micelles under shear," J. Phys. II **4**, 1261–1279 (1994).

Bhave, A. V., R. C. Armstrong, and R. A. Brown, "Kinetic theory and rheology of dilute, nonhomogeneous

polymer solutions," J. Chem. Phys. **95**, 2988–3000 (1991).
Boukany, P. E., Y. T. Hu, and S. Q. Wang, "Observations of wall slip and shear banding in an entangled DNA solution," Macromolecules **41**, 2644–2650 (2008).
Cannavacciuolo, L., J. S. Pedersen, and P. Schurtenberger, "Monte Carlo simulation study of concentration effects and scattering functions for polyelectrolyte wormlike micelles," Langmuir **18**, 2922–2932 (2002).
Cappelaere, E., J. F. Berret, J. P. Decruppe, R. Cressely, and P. Lindner, "Rheology, birefringence, and small-angle neutron scattering in a charged micellar system: Evidence of a shear-induced phase transition," Phys. Rev. E **56**, 1869–1878 (1997).
Cappelaere, E. and R. Cressely, "Shear banding structure in viscoelastic micellar solutions," Colloid Polym. Sci. **275**, 407–418 (1997).
Cappelaere, E., R. Cressely, and J. P. Decruppe, "Linear and nonlinear rheological behavior of salt-free aqueous CTAB solutions," Colloids Surf., A **104**, 353–374 (1995).
Cates, M. E. and S. J. Candau, "Statics and dynamics of worm-like surfactant micelles," J. Phys.: Condens. Matter **2**, 6869–6892 (1990).
Decruppe, J. P., R. Cressely, R. Makhloufi, and E. Cappelaere, "Flow birefringence experiments showing a shear-banding structure in a CTAB solution," Colloid Polym. Sci. **273**, 346–351 (1995).
Dhont, J. K. G. and W. J. Briels, "Gradient and vorticity banding," Rheol. Acta **47**, 257–281 (2008).
Douglass, B. S., R. H. Colby, L. A. Madsen, and P. T. Callaghan, "Rheo-NMR of wormlike micelles formed from nonionic pluronic surfactants," Macromolecules **41**, 804–814 (2008).
Eppenga, R. and D. Frenkel, "Monte Carlo study of the isotropic and nematic phases of infinitely thin hard platelets," Mol. Phys. **52**, 1303–1334 (1984).
Fielding, S. M. and P. D. Olmsted, "Flow phase diagrams for concentration-coupled shear banding," Eur. Phys. J. E **11**, 65–83 (2003).
Fischer, E. and P. T. Callaghan, "Is a birefringence band a shear band?" Europhys. Lett. **50**, 803–809 (2000).
Fischer, E. and P. T. Callaghan, "Shear banding and the isotropic-to-nematic transition in wormlike micelles," Phys. Rev. E **64**, 011501 (2001).
Ganapathy, R. and A. K. Sood, "Nonlinear flow of wormlike micellar gels: Regular and chaotic time-dependence of stress, normal force and nematic ordering," J. Non-Newtonian Fluid Mech. **149**, 78–86 (2008).
Giesekus, H., "A simple constitutive equation for polymer fluids based on the concept of deformation-dependent tensorial mobility," J. Non-Newtonian Fluid Mech. **11**, 69–109 (1982).
Glinka, C. J., J. G. Barker, B. Hammouda, S. Krueger, J. J. Moyer, and W. J. Orts, "The 30 m small-angle neutron scattering instruments at the National Institute of Standards and Technology," J. Appl. Crystallogr. **31**, 430–445 (1998).
Gortemaker, F. H., M. G. Hansen, B. D. Cindio, H. M. Laun, and H. Janeschitzkriegl, "Flow birefringence of polymer melts—application to investigation of time-dependent rheological properties," Rheol. Acta **15**, 256–267 (1976).
Hertel, G. and H. Hoffmann, "Lyotropic nematic phases of double chain surfactants," Prog. Colloid Polym. Sci. **76**, 123–131 (1988).
Holmes, W. M., P. T. Callaghan, D. Vlassopoulos, and J. Roovers, "Shear banding phenomena in ultrasoft colloidal glasses," J. Rheol. **48**, 1085–1102 (2004).
Hu, Y. T. and A. Lips, "Kinetics and mechanism of shear banding in an entangled micellar solution," J. Rheol. **49**, 1001–1027 (2005).
Hu, Y. T., C. Palla, and A., Lips "Comparison between shear banding and shear thinning in entangled micellar solutions," J. Rheol. **52**, 379–400 (2008).
Hu, Y. T., L. Wilen, A. Philips, and A. Lips, "Is the constitutive relation for entangled polymers monotonic?" J. Rheol. **51**, 275–295 (2007).
Imae, T., "Light scattering of spinnable, viscoelastic solutions of hexadecyltrimethylammonium salicylate," J. Phys. Chem. **94**, 5953–5959 (1990).
Joo, Y. L., J. Sun, M. D. Smith, R. C. Armstrong, R. A. Brown, and R. A. Ross, "Two-dimensional numerical analysis of non-isothermal melt spinning with and without phase transition," J. Non-Newtonian Fluid Mech. **102**, 37–70 (2002).

25 October 2023 01:47:23

Larson, R. G., in *The Structure and Rheology of Complex Fluids. Topics in Chemical Engineering*, edited by Gubbins, K. E. (Oxford University Press, New York, 1999), p. 663.

Lee, J. Y., G. G. Fuller, N. E. Hudson, and X. F. Yuan, "Investigation of shear-banding structure in wormlike micellar solution by point-wise flow-induced birefringence measurements," J. Rheol. **49**, 537–550 (2005).

Liberatore, M. W., F. Nettesheim, E. W. Kaler, M. E. Helgeson, N. J. Wagner, P. A. Vasquez, L. P. Cook, Y. T. Hu, and L. Porcar, "Microstructure and shear rheology of entangled wormlike micelles in solution," J. Rheol. **53**, 441–458 (2009).

Liberatore, M. W., F. Nettesheim, N. J. Wagner, and L. Porcar, "Spatially resolved small-angle neutron scattering in the 1-2 plane: A study of shear-induced phase-separating wormlike micelles," Phys. Rev. E **73**, 020504(R) (2006).

López-González, M. R., W. M. Holmes, and P. T. Callaghan, "Rheo-NMR phenomena of wormlike micelles," Soft Matter. **2**, 855–869 (2006).

Manneville, S., A. Colin, G. Waton, and F. Schosseler, "Wall slip, shear banding, and instability in the flow of a triblock copolymer micellar solution," Phys. Rev. E **75**, 061502 (2007).

Miller, E. and J. P. Rothstein, "Transient evolution of shear-banding wormlike micellar solutions," J. Non-Newtonian Fluid Mech. **143**, 22–37 (2007).

Nettesheim, F., M. W. Liberatore, T. K. Hodgdon, N. J. Wagner, E. W. Kaler, and M. Vethamuthu, "Influence of nanoparticle addition on the properties of wormlike micellar solutions," Langmuir **24**, 7718–7726 (2008).

Olmsted, P. D., "Perspectives on shear banding in complex fluids," Rheol. Acta **47**, 283–300 (2008).

Pedersen, J. S. and P. Schurtenberger, "Scattering functions of semiflexible polymers with and without excluded volume effects," Macromolecules **29**, 7602–7612 (1996).

Rehage, H. and H. Hoffmann, "Viscoelastic surfactant solutions—model systems for rheological research," Mol. Phys. **74**, 933–973 (1991).

Rossi, L. F., G. McKinley, and L. P. Cook, "Slippage and migration in Taylor–Couette flow of a model for dilute wormlike micellar solutions," J. Non-Newtonian Fluid Mech. **136**, 79–92 (2006).

Schubert, B. A., E. W. Kaler, and N. J. Wagner, "The microstructure and rheology of mixed cationic/anionic wormlike micelles," Langmuir **19**, 4079–4089 (2003).

Schubert, B. A., N. J. Wagner, E. W. Kaler, and S. R. Raghavan, "Shear-induced phase separation in solutions of wormlike micelles," Langmuir **20**, 3564–3573 (2004).

Shikata, T., S. J. Dahman, and D. S. Pearson, "Rheooptical behavior of wormlike micelles," Langmuir **10**, 3470–3476 (1994).

Spenley, N. A., M. E. Cates, and T. C. B. McLeish, "Nonlinear rheology of wormlike micelles," Phys. Rev. Lett. **71**, 939–942 (1993).

Vasanthi, R., S. Ravichandran, and B. Bagchi, "Anisotropic diffusion of tagged spheres near the isotropic-nematic phase transition," J. Chem. Phys. **115**, 10022–10028 (2001).

Vasquez, P. A., G. H. McKinley, and L. P. Cook, "A network scission model for wormlike micellar solutions—I. Model formulation and viscometric flow predictions," J. Non-Newtonian Fluid Mech. **144**, 122–139 (2007).

Vermant, J. and M. J. Solomon, "Flow-induced structure in colloidal suspensions," J. Phys.: Condens. Matter **17**, R187–R216 (2005).

Wagner, N. J., M. Liberatore, F. Nettesheim, and L. Porcar, "Small angle neutron scattering under flow in the 1-2 plane: Rheo-SANS of phase-separating self-assembled wormlike surfactants," Abstr. Pap.-Am. Chem. Soc. **230**, 462–ANYL (2005).

Walker, L. M. and N. J. Wagner, "SANS analysis of the molecular order in poly(gamma-benzyl L-glutamate) deuterated dimethylformamide (PBLG/d-DMF) under shear and during relaxation," Macromolecules **29**, 2298–2301 (1996).

Wiest, J. M. and R. B. Bird, "Molecular extension from the Giesekus model," J. Non-Newtonian Fluid Mech. **22**, 115–119 (1986).

Yesilata, B., C. Clasen, and G. H. McKinley, "Nonlinear shear and extensional flow dynamics of wormlike surfactant solutions," J. Non-Newtonian Fluid Mech. **133**, 73–90 (2006).

Zhou, L., P. A. Vasquez, L. P. Cook, and G. H. McKinley, "Modeling the inhomogeneous response and formation of shear bands in steady and transient flows of entangled liquids," J. Rheol. **52**, 591–623 (2008).

25 October 2023 01:47:23